Target Identification with Wave-Based Matched Pursuits and Hidden Markov Models

Priya K. Bharadwaj, Paul R. Runkle, and Lawrence Carin, *Senior Member, IEEE*

***Abstract*—The method of matched pursuits is an algorithm by which a waveform is parsed into its fundamental constituents here, in the context of short-pulse electromagnetic scattering, wavefronts, and resonances (constituting what we have called *wave-based* matched pursuits). The wave-based matched-pursuits algorithm is used to develop a codebook of features that are representative of time-domain scattering from a target of interest, accounting for the variability of such as a function of target-sensor orientation. This codebook is subsequently used in the context of a hidden Markov model (HMM) in which the probability of measuring a particular codebook element is quantified as a function of target-sensor orientation. We review the wave-based matched-pursuits algorithm and its use in the context of an HMM (for target identification). Finally, this new wave-based signal processing algorithm is demonstrated with simulated scattering data, with additive noise.**

***Index Terms*—Electromagnetic scattering, target identification.**

I. Introduction

THE use of scattered fields to infer the identification of a distant or concealed target constitutes a problem of longstanding interest. In the context of wide-band or time-domain scattering, there has been significant interest in the use of late-time resonances [1]–[4] as a means of target identification. Such research has been motivated by Baum's [1] singularity expansion method (SEM), which represents the late-time scattered fields in terms of a sum of resonances, each of which has an excitation independent resonant frequency (although the modal excitation strengths *are* aspect dependent).

The resonant frequencies of many targets are very low Q and, hence, difficult to extract from noisy data. Therefore, researchers have investigated detection and identification algorithms based on wavefronts scattered from localized target scattering centers [5]–[10]. The time of arrival of consecutive wavefronts yields important information on the target size, while the frequency dependence of the wavefronts can be used for scattering-center identification [6]–[10]. In particular, from the geometrical theory of diffraction (GTD) [5], the frequency dependence of many canonical scattering centers (edges, corners, finite plates, *etc.*) have been catalogued [6] and can therefore be used to identify features on the target, with the cumulative information from multiple scattering centers yielding information about the global target itself. This approach has been investigated by several authors, using model-based or "super-resolution" algorithms [6], [8]–[10], and Cramer–Rao bound studies have quantified the (relatively high) signal-to-noise ratio (SNR) required to make such an approach viable [6].

Wide-band electromagnetic scattering from most realistic targets cannot be characterized by wavefronts or resonances independently, but rather by a combination of wavefronts and resonances, with the relative importance of each dependent on the target and the target-sensor orientation. Therefore, the SEM and GTD algorithms discussed above are each only applicable to a subclass of possible wave phenomenology. Consequently, of late, several investigators have considered time-frequency algorithms [11]–[19]. Such algorithms represent wavefronts as features with narrow support in time and wide support in frequency while representing resonant wave objects in a complementary manner. In the context of time-frequency algorithms, researchers have considered windowed Fourier transforms [11], [13], [15], wavelet transforms [12], [16], [17], and matched pursuits [18]. The matched-pursuits algorithm with a Gabor dictionary has been used to parse wide-band scattering data into its wavefront and resonant constituents—the former used subsequently to form an inverse synthetic radar (ISAR) image (devoid of resonant artifacts) and the latter used for resonant-feature identification [19].

In the research described here, we present a new strategy by which wavefronts and resonances are used *simultaneously* to effect target identification. In particular, instead of using matched pursuits with a Gabor dictionary [20], we utilize our understanding of the underlying physics to constitute a wave-based dictionary [18] composed of wavefronts and resonances [2]. Moreover, we utilize the wave-based matched-pursuits algorithm in the context of a hidden Markov model (HMM) to effect target identification. The utilization of an HMM framework is motivated by the extensive use of the HMM paradigm in speech processing (word identification), where it has been applied with notable success [21]–[29].

It is well known that the fields scattered from a general target are a strong function of the target-sensor orientation. However, there are generally angular sectors over which the scattering physics is slowly varying. For example, consider a hollow conducting sphere, with a hole in the sphere allowing access to the internal cavity. At target-sensor orientations for which electromagnetic energy is efficiently coupled into the internal cavity, the scattered fields may be dominated by resonant scattering (depending on the excitation bandwidth and the cavity resonant frequencies). At the other target-sensor orientations, for which there is weak coupling, the scattered fields will be dominated principally by wavefront

Manuscript received May 22, 1998; revised June 3, 1999. This work was supported in part by the Office of Naval Research under Grant N00014-96-1-0861.

The authors are with the Department of Electrical and Computer Engineering, Duke University, Durham, NC 27708 USA.

Publisher Item Identifier S 0018-926X(99)09383-7.

(nonresonant) scattering. Moving from this simple example to scattering from a general target, we similarly can divide the target-sensor orientations into angular sectors over which a particular class of physics dominates. We term each such angular sector a target "state." The number of states required to characterize scattering from a given target is dependent on the target complexity and sensor bandwidth.

Assume that the fields scattered from a target are measured from multiple target-sensor orientations, due to sensor motion, target motion, or both. The target identity and orientation are assumed unknown. Within the context of the above terminology, the multiple scattered waveforms sample multiple states of the target under interrogation, where the same state may be sampled more than once and other states not at all, depending on the details of the target-sensor motion (the particular states so sampled are "hidden," because the target is assumed concealed or distant). Let q_m represent the state sampled on the mth measurement. We demonstrate in Section III that for M such measurements, the sequence of sampled states $\{q_1, q_2, \cdots, q_M\}$ can be modeled statistically as a Markov chain.

The M-scattered waveforms are parsed into a set of features via wave-based matched pursuits, where $\boldsymbol{u}_m$ represents the feature vector for the mth scattered waveform. The ensemble of scattered waveforms associated with state q_m are characterized by a corresponding ensemble of feature vectors, with $\boldsymbol{u}_m$ representing one realization of such. The selection of $\boldsymbol{u}_m$ from that ensemble can also be viewed as a random process. Hence, the extraction of the *sequence* of feature vectors $\{\boldsymbol{u}_1, \boldsymbol{u}_2, \cdots, \boldsymbol{u}_M\}$ is representative of a *doubly stochastic* process: 1) sampling of multiple target states $\{q_1, q_2, \cdots, q_M\}$ with such treated statistically due to the unknown target orientation and 2) for each state so sampled, extraction of particular feature vectors yielding the sequence $\{\boldsymbol{u}_1, \boldsymbol{u}_2, \cdots, \boldsymbol{u}_M\}$. Note that the same state sequence $\{q_1, q_2, \cdots, q_M\}$ can yield distinct realizations of the feature vectors $\{\boldsymbol{u}_1, \boldsymbol{u}_2, \cdots, \boldsymbol{u}_M\}$. Further, in practice we only have access to the feature vectors $\{\boldsymbol{u}_1, \boldsymbol{u}_2, \cdots, \boldsymbol{u}_M\}$, with the associated state sequence $\{q_1, q_2, \cdots, q_M\}$ "hidden." Consequently, as demonstrated in Section III, such a doubly stochastic process is well characterized via a *hidden* Markov model (HMM).

Note that the basic *identification* strategy invoked here is based on viewing target scattering from multiple (hidden) target sensor orientations, with the consequent multiple waveforms characterized by an HMM. This multi-aspect target identification strategy is consistent with mammalian identification of prey [30]–[32] and is also consistent with the multi-aspect data implicitly utilized in SAR [33], ISAR [34], and inverse scattering [35]. Finally, we note that in addition to accounting for the underlying wave phenomenology, the HMM construct involves a "training" phase, forming a *statistical* link between the wave physics and the variability of such in actual target scattering. In this connection, the HMM is related to neural networks [36], which also exploit a training phase. However, while neural networks *implicitly* account for the wave physics during training, here, in the context of physics-based HMM's, this connection is made *explicit.*

The remainder of the text is organized as follows. In Section II, we give a brief review of the wave-based matched-pursuits algorithm [18], [37], which provides data parsing during both training and testing. The HMM framework is detailed in Section III, in which we elucidate codebook generation, formulation of associated states, as well as various associated statistical measures. Example results are presented in Section IV, followed by conclusions in Section V.

II. Wave-Based Matched Pursuits

A. Algorithm Basics

The matched-pursuits algorithm [20] utilizes a dictionary of fundamental elements $\boldsymbol{e}(\gamma)$, where γ represents the associated vector parameters. The dictionary is initially discretized into N normalized vectors $\boldsymbol{e}(\gamma_n)$, where the γ_n represent N realizations of the general parameter vector γ. Given a sampled waveform $\boldsymbol{f}$, we form the inner product $\langle \boldsymbol{f} | \boldsymbol{e}(\gamma_n) \rangle$ with each discretized element $\boldsymbol{e}(\gamma_n)$ in the finite-size dictionary D. The inner product of vectors $\boldsymbol{f}$ and $\boldsymbol{e}(\gamma_n)$ is defined as $\langle \boldsymbol{f} | \boldsymbol{e}(\gamma_n) \rangle = \boldsymbol{f}[\boldsymbol{e}(\gamma_n)]^H$ where superscript H represents the Hermitian transpose and $|\boldsymbol{f}|^2 = \langle \boldsymbol{f} | \boldsymbol{f} \rangle$. We select that $\boldsymbol{e}(\gamma_n)$ for which $|\langle \boldsymbol{f} | \boldsymbol{e}(\gamma_n) \rangle| \geq |\langle \boldsymbol{f} | \boldsymbol{e}(\gamma_k) \rangle| \forall\, \boldsymbol{e}(\gamma_k) \in D$. A gradient search in the γ space is then performed in the vicinity of γ_n from which we find the γ that maximizes the inner product $|\langle \boldsymbol{f} | \boldsymbol{e}(\gamma) \rangle|$ defining the associated vector $\hat{\boldsymbol{e}}_1$. We now have the representation

$$\boldsymbol{f} = \langle \boldsymbol{f} | \hat{\boldsymbol{e}}_1 \rangle \hat{\boldsymbol{e}}_1 + \boldsymbol{R}_1 \tag{1}$$

where $\boldsymbol{R}_1$ is the remainder after the first iteration ($\langle \boldsymbol{R}_1 | \hat{\boldsymbol{e}}_1 \rangle = 0$). This process is now repeated, but instead of operating on $\boldsymbol{f}$, we perform inner products of the elements in D with $\boldsymbol{R}_1$ followed by the associated gradient search in the γ space. After K such matched-pursuits iterations, we have

$$\boldsymbol{f} = \sum_{k=1}^{K} \langle \boldsymbol{R}_{k-1} | \hat{\boldsymbol{e}}_k \rangle \hat{\boldsymbol{e}}_k + \boldsymbol{R}_K \tag{2}$$

where $\boldsymbol{R}_0 \equiv \boldsymbol{f}$. Moreover, we have the energy balance

$$|\boldsymbol{f}|^2 = \sum_{k=1}^{K} |\langle \boldsymbol{R}_{k-1} | \hat{\boldsymbol{e}}_k \rangle|^2 + |\boldsymbol{R}^K|^2. \tag{3}$$

If the vectors represented by D with the associated gradient search constitute a complete set, then $|\boldsymbol{R}_K| \to 0$ as $K \to \infty$. However, for our purposes we are not interested in a complete decomposition of the signal $\boldsymbol{f}$, rather, we wish to use a relatively small number of iterations K to extract the principal constituents $\hat{\boldsymbol{e}}_k$ most representative of $\boldsymbol{f}$. As discussed further below, in the context of the HMM for the data we have considered here, we typically use K on the order of two or three.

B. Wave-Based Dictionary

The algorithm discussed above can be utilized with a general dictionary D, Gabor basis functions representing a popular choice [20]. However, for electromagnetic scattering applications, it is natural to tailor the dictionary to the underlying

wave physics. To this end, we introduce the discrete-time dictionary elements

$$\begin{aligned} \boldsymbol{e}(i;\, p,\, l,\, \nu,\, \phi) &= \cos\left[2\pi(i-\nu 2^{p-1} l 2^{-p}+\phi\right] \\ &\quad \cdot \exp\left[-(i-\nu 2^{p-1})2^{-p}\right] U(i-\nu 2^{p-1}) \\ &\quad p = \log_2 N_i, \cdots, \log_2(\xi N_i) \\ &\quad l = 0, \cdots, 2^p - 1 \\ &\quad \nu = 0, \cdots, N_s 2^{1-p} \end{aligned} \tag{4}$$

where $U(\beta) = 0$ for $\beta < 0$ and $U(\beta) = 1$ for $\beta \geq 0$, N_s represents the number of samples in the data under investigation, N_i is the nominal number of meaningful (nonzero) time samples in the incident pulse and ξN_i represents the largest expected length for a resonant waveform (typically we utilize $\xi = 8$). In (4), p and ν take on integer values and, therefore, the logarithms and quotients in (4) are rounded off accordingly, if necessary. The sampling paradigm for p, l, and ν is analogous to that applied in [20] for a Gabor dictionary, but here in the context of our wave-based dictionary, we assure that the minimum envelope width is no smaller than the width of the incident excitation and the maximum width is consistent with the longest-duration resonance that may be realistically excited. Note that (4) is in its unnormalized form, while in the actual matched-pursuits implementation all vectors in D are normalized appropriately.

For the finite dictionary D used in the initial matched-pursuits search (before performing gradient optimization of the parameters γ), we utilize the *complex* vectors

$$\begin{aligned} \boldsymbol{e}_c(i;\, p,\, l,\, \nu) &= \exp\left[j2\pi(i-\nu 2^{p-1})l 2^{-p}\right] \\ &\quad \cdot \exp\left[-(i-\nu 2^{p-1})2^{-p}\right] U(i-\nu 2^{p-1}) \end{aligned} \tag{5}$$

where $j = (-1)^{1/2}$. In a manner similar to that discussed in [20], the phase ϕ is estimated while forming inner products with the initial coarsely sampled $\boldsymbol{e}_c$ and then p, l, q, and ϕ (i.e., the parameters γ) are refined subsequently via the gradient search [performed using the *real* vectors $\boldsymbol{e}$ in (4)].

III. Hidden Markov Model Formulation

A. Codebook Development and Vector Quantization

The first issue of interest in the HMM algorithm is characterizing the statistical distribution of the state-dependent feature vectors $\boldsymbol{u}$. Various time-frequency algorithms have been investigated for generation of feature vectors [38], [39], but here in the context of electromagnetic scattering, we invoke the wave-based matched-pursuits algorithm outlined in Section II. In particular, after K matched pursuits iterations on a given scattered waveform, we extract the parameter vector $\boldsymbol{u} = \{\omega_1, \alpha_1, t_2 - t_1, \omega_2, \alpha_2, \cdots, t_K - t_1, \omega_K, \alpha_K\}$. This vector stores the angular frequency and decay constant extracted on each matched-pursuits iteration ($\alpha = 2^p$ and $\omega = 2\pi l/\alpha$), as well as the timing ($t = \nu 2^{p-1}$) relative to t_1. The parameters t_1, ω_1, α_1 correspond to the wave-object occurring earliest in time, while t_K, ω_K, α_K correspond to the wave-object occurring latest. The remaining parameters in $\boldsymbol{u}$ are arranged consecutively with time. In $\boldsymbol{u}$ we utilize *relative* times because such are only dependent upon the target geometry (and the target-sensor orientation), while the absolute arrival times are dependent on the (variable) target-sensor distance. The vector $\boldsymbol{u}$ essentially represents a parsing of the scattered waveform in terms of the wavefront-resonance dictionary discussed in Section II. This compact representation, in terms of $3K - 1$ parameters, should be contrasted with storage of the original waveform of N_s samples (in most examples $N_s \gg 3K-1$). Moreover, in the actual HMM implementation we may utilize only a subset of these $3K-1$ components (those that are less susceptible to noise, for example).

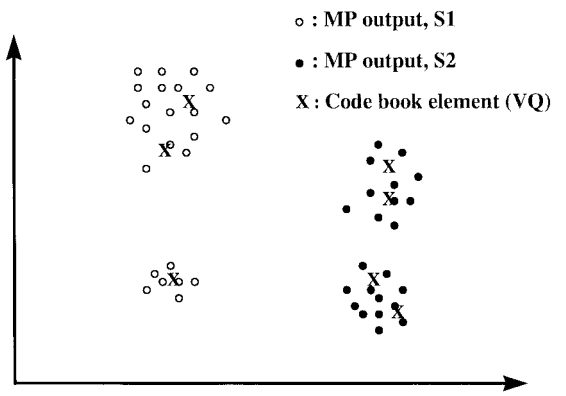

Fig. 1. Illustration of features in a general 2-D phase space, extracted via matched pursuits (MP). The solid and open circles are representative of different "states" (target-sensor orientations, denoted here S1 and S2), in which the underlying physics is different. The "X" symbols identify possible codebook elements, which collectively seek to model the distribution of extracted features in the phase space. This figure is only "illustrative" (not representative of real data); in general, the number of clusters associated with a give state is problem dependent.

The vector $\boldsymbol{u}$ resides in the $3K - 1$ dimensional space. To determine the regions in that space most representative of scattering from a given target, we perform wave-based matched pursuits on all available scattered waveforms from said target (sampling the range of target-sensor orientations expected in practice). For Λ observation angles, we obtain Λ vectors $\boldsymbol{u}_1, \boldsymbol{u}_2, \cdots, \boldsymbol{u}_\Lambda$, which constitute the distribution of the $3K - 1$ parameters for the target of interest. The statistics of the continuous feature vectors $\boldsymbol{u}_1, \boldsymbol{u}_2, \cdots, \boldsymbol{u}_\Lambda$ are generated via a discrete approximation. In particular, we define a finite number (N_c) of vectors in the $3K - 1$ parameter space, with the N_c discrete feature vectors termed a "codebook," and each individual element is called a "codebook element." Each continuous feature vector $\boldsymbol{u}$ is mapped, in a nearest-neighbor sense, to a particular codebook element. The probability distribution of the continuous feature space is quantified approximately via a discretized histogram, defined as the probability of witnessing each codebook element (after nearest-neighbor mapping), for the target of interest. The number of codebook elements N_c is designed such that $N_c \ll \Lambda$. This procedure is demonstrated schematically in Fig. 1, for a two-dimensional (2-D) slice in the $3K-1$ dimensional space (this figure is purely for illustrative purposes).

This discretization of the continuous feature space is termed vector quantization (VQ). A simple VQ example is discussed for clarity. Assume that the voltage output of some device is known to range between zero and $V_{\max}$. Further, we wish to quantize the output voltage in terms of N_c discrete values. For

a given N_c, the objective is to determine which N_c discrete voltage values are best used for this quantization problem. We can start by defining N_c discrete voltages, uniformly distributed between zero and $V_{\max}$ (this is our initial "codebook"). During the "training" phase, many voltage measurements are performed. Using a nearest-neighbor mapping, we associate each training voltage with the discrete voltage (of N_c possible) to which it is closest. This is the "clustering" phase. For the cluster of training voltages associated with a given codebook element, we update the corresponding codebook element as the average of all voltages in the respective cluster. This is done for all N_c initial codebook elements. Using the same training data, the process is then repeated, with the iterative process terminated after the set of codebook elements achieve convergence (the change in the codebook is below a specified threshold). Subsequently, in the "testing" phase, each measured voltage is mapped to one of the discrete codebook elements, again in the nearest-neighbor sense. The probability of achieving a voltage from zero to $V_{\max}$ is approximated via a histogram using the training data and the discrete set of codebook elements.

Focusing again on the target-classification problem of interest here, there are two related issues that need be addressed: 1) determination of the optimal codebook $\hat{\boldsymbol{u}}_1, \hat{\boldsymbol{u}}_2, \cdots, \hat{\boldsymbol{u}}_{Nc}$ for representation of the training data $\boldsymbol{u}_1, \boldsymbol{u}_2, \cdots, \boldsymbol{u}_\Lambda$ (from Λ observation angles) and 2) after the codebook is so defined, the mapping from a general measured parameter vector $\boldsymbol{u}$ to the appropriate codebook element $\hat{\boldsymbol{u}}_k$. Issue 1) is termed "populating the codebook" [38], [39], implemented during the training phase and 2) addresses how each codebook element is assigned, during the testing phase (i.e., when the scattered waveform from an unknown target is used in the context of target identification). There is a vast VQ literature [38]–[40], while here, for completeness, we only address the fundamental issues in VQ as well as the particular VQ algorithm applied.

We begin by defining a distortion or distance metric $d(\boldsymbol{u}, \hat{\boldsymbol{u}})$, where we utilize the Mahalanobis distance [41]

$$d(\boldsymbol{u}, \hat{\boldsymbol{u}}) = (\boldsymbol{u}-\hat{\boldsymbol{u}})^T C^{-1}(\boldsymbol{u}-\hat{\boldsymbol{u}}), \quad \text{with } C = E[(\boldsymbol{u}-\overline{\boldsymbol{u}})(\boldsymbol{u}-\overline{\boldsymbol{u}})^T] \tag{6}$$

where C is the covariance matrix and $\overline{\boldsymbol{u}} = E(\boldsymbol{u})$ (each of which we estimate through averaging over the available vectors $\boldsymbol{u}$). The expression in (6) is termed a distortion measure because it represents the perturbation to a measured vector $\boldsymbol{u}$ when it is quantized to $\hat{\boldsymbol{u}}$. While (6) is the most popular such metric, there are several alternatives in the literature [40]. Moreover, from our discussion of the matched-pursuits algorithm, the vectors $\boldsymbol{u}$ and $\hat{\boldsymbol{u}}$ in (6) are assumed to be of length $3K-1$. However, as mentioned previously, one could utilize a subset of the $3K-1$ matched-pursuits parameters if desired.

For a codebook of vectors $\hat{\boldsymbol{u}}_1, \hat{\boldsymbol{u}}_2, \cdots, \hat{\boldsymbol{u}}_{Nc}$, VQ is effected via the quantization operator $g(\cdot)$, where

$$\hat{\boldsymbol{u}}_k = g(\boldsymbol{u}) \quad \text{iff } d(\boldsymbol{u}, \hat{\boldsymbol{u}}_k) \le d(\boldsymbol{u}, \hat{\boldsymbol{u}}_i) \quad \forall\, 1 \le i \le N_c \tag{7}$$

which is essentially a "nearest-neighbor" mapping. While this solution to issue 2) is relatively straightforward and intuitive, there are several different algorithms available for generation of the codebook itself. The interested reader is referred to [40] for an excellent summary of the various methods available for codebook generation, while we focus on the particular algorithm applied here, referred to as the K-means [39] or Linde, Buzo and Gray (LBG) [39] algorithm. The algorithm is implemented via the following four steps: a) define an initial codebook of N_c vectors, which provides a reasonable starting point; b) using the metric in (7), cluster (associate) each of the training vectors $\boldsymbol{u}_1, \boldsymbol{u}_2, \cdots, \boldsymbol{u}_\Lambda$ with a particular codebook element with C_k representing the cluster of training vectors associated with the kth codebook element; c) update the codebook elements by defining the new codebook vector $\hat{\boldsymbol{u}}_k'$ associated with cluster C_k, where

$$\boldsymbol{u}_k' = \frac{1}{N_k} \sum_{\boldsymbol{u}_n \in C_k} \boldsymbol{u}_n \tag{8}$$

is the cluster centroid, with N_k representing the number of training vectors in C_k; and d) with the updated codebook, compute the average distortion for all training vectors, relative to the codebook to which they are assigned. If the distortion (or change in distortion) is below a prescribed value, the codebook generation is complete, if not, return to b). The detailed mathematical characteristics of this algorithm have been examined extensively [39], [40]. With regard to step a) in which the starting codebook is defined, one can spread the initial codebook entries uniformly within the parameter space or, based on *a priori* knowledge (of the target and underlying scattering physics), the initial codebook can be linked to anticipated wave phenomenology.

B. Hidden Markov Model (HMM) Implementation

Above we have introduced the concept of a codebook for quantization of the continuous feature space. For target identification, we are interested in the probability of realizing each codebook element, for targets of interest. This issue is complicated by the fact that, as discussed in the introduction, the wave physics is generally a strong function of the target-sensor orientation. Therefore, for a given target, the probability of witnessing particular codebook elements is also target-sensor-orientation dependent. This issue, as discussed below, is handled within the context of a hidden Markov model (HMM).

When testing the identification of a concealed or distant target, we assume we have access to M measured waveforms, from M different target-sensor orientations. While the *relative* angles between the M measurements are known, the absolute target-sensor angles (orientations) are not (i.e., they are "hidden"), because the target cannot be seen. For each of the M measured waveforms, K wave-based matched-pursuits iterations are performed from which we obtain the M parameter vectors $\boldsymbol{u}_1, \boldsymbol{u}_2, \cdots, \boldsymbol{u}_M$, these vectors, in general, being different from or a subset of the Λ vectors are used to populate the codebook. Matched pursuits is followed by VQ from which the M vectors (with, in general, continuous parameters) are mapped to M discrete codebook elements, constituting the observation vector $\boldsymbol{O} = \{O_1, O_2, \cdots, O_M\}$ (each discrete observation O_k represents one of the codebook elements). From the Introduction, the M measurements correspond to sampling scattered waveforms from the states of the target, where q_m

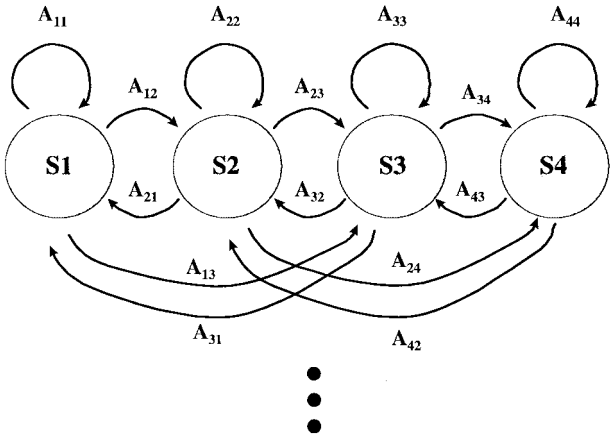

Fig. 2. Schematization of a four-state hidden Markov model (HMM). The A_{ij} represent the probability of transitioning from state i to state j. In general, all state transitions have nonzero probability of occurrence; the figure only shows a subset of all possible transitions.

represents the state sampled for measurement m. However, the state sequence $\{q_1, q_2, \cdots, q_M\}$ associated with $\boldsymbol{O}$ is hidden, and, therefore, we model the statistics of $\boldsymbol{O}$ via a *hidden* Markov model (HMM). An HMM is constructed for each target of interest, and the target is identified as that for which the observation vector $\boldsymbol{O}$ has the highest *probability* of occurring.

Assume a target of interest has M_s states, each of which constitutes a range of angles (target-sensor orientations) over which the wave physics is relatively invariant, i.e., angular regions for which the parameter vectors $\boldsymbol{u}$ extracted via matched pursuits are highly correlated. In Fig. 2, we show, for example, a four-state HMM model ($M_s = 4$), implying that wave scattering from the target in question can be partitioned into four principal domains or target-sensor orientations. The HMM is characterized by the matrices $\boldsymbol{A}$ and $\boldsymbol{B}$ and by the vector π. The $M_s \times M_s$ matrix $\boldsymbol{A}$ represents the state-transition probabilities. For example, A_{ik} represents the probability that there will be a transition from state i to state k (as one moves the angle of observation) [42]. Since the states represent angular domains, the probabilities A_{ik} are dictated largely by geometry. The $N_c \times M_s$ matrix $\boldsymbol{B}$ represents the probability that each codebook element will be observed in a given state, i.e., B_{ik} represents the probability that codebook element i is observed in state k (referring to Section III-A, we see that the probability of witnessing a given codebook element is not simply a function of the target in question, but also of the state—target-sensor orientation—being sampled for that target). Finally, the M_s-dimensional vector π represents the probability that the initial observation is in each of the states and, therefore, π_k represents the probability that the initial observation (scattered waveform) corresponds to state k. The vector π is, therefore, also dictated largely by geometry.

For a model with M_s states and M angular observations, the probability that the sequence of codebook vectors $\boldsymbol{O}$ is observed for HMM model $\boldsymbol{M}$ is given by

$$p(\boldsymbol{O}|\boldsymbol{M}) = \sum_{k=1}^{M_s} \pi_k B_k(O_1) \sum_{i=1}^{M_s} A_{ki} B_i(O_2) \sum_{n=1}^{M_s} A_{in} B_n(O_3) \cdots \sum_{l=1}^{M_s} A_{pl} B_l(O_M) \tag{9}$$

where $B_i(O_k)$ is an element in $\boldsymbol{B}$, representing the probability that codebook element O_k is observed in state i (where O_k is the codebook extracted after VQ for the kth angular observation). There are simple algorithms available in the literature by which (9) is computed efficiently [22], [23], [43].

What remains to be discussed are the details of how one determines the probabilities $\boldsymbol{A}$, $\boldsymbol{B}$ and π. Recall that the HMM states can be attributed to target-sensor orientations for which the scattering phenomenology is largely unchanged. Through *a priori* knowledge of the target and associated scattering, one can often delineate where such states will reside (this can also be inferred by examination of which parameters are selected via the wave-based matched pursuits algorithm, as a function of target-sensor orientation). Therefore, it is relatively straightforward (as will be demonstrated in the examples) to determine which angular domains should constitute a state. Once this partitioning is accomplished, the probabilities in the vector π are available immediately from geometry (assuming that all target-sensor orientations are equally likely). Moreover, the transition probabilities $\boldsymbol{A}$ are readily computed from the rate of angular change (between each of the M orientation-dependent measurements) and knowledge of how the states are partitioned geometrically. Rigorously speaking, the matrix elements in $\boldsymbol{A}$ are time dependent based on previous state transitions; for example, if two consecutive observations remain in the same state, the probability of transitioning out of that state is higher than if this is not the case. Time-dependent $\boldsymbol{A}$ matrices have been considered in speech processing [26], [27] and will constitute the subject of future research in the context of target identification.

Finally, the matrix $\boldsymbol{B}$ represents the probability that within a given state, VQ will lead to the selection of a particular codebook element. Again, since the states are linked to known target-sensor orientations, training can be effected (via wave-based matched pursuits followed by VQ), to determine the probability of selecting each codebook element for a given state. While the number of independent orientation-dependent scattered waveforms is clearly limited, further training (on a fixed set of scattering data) can be affected by adding noise to the data from which an unlimited set of noisy data can be generated.

The explicit method employed to compute $\boldsymbol{A}$, $\boldsymbol{B}$, and π is discussed in the Appendix. These initial probabilities are subsequently refined using techniques that have been developed in the speech processing community [22], [23], [43]. In particular, given observations $\boldsymbol{O}$ from a given target, we refine the probabilities $\boldsymbol{A}$, $\boldsymbol{B}$ and π such that $p(\boldsymbol{O}|\boldsymbol{M})$ is maximized, where $\boldsymbol{M}$ corresponds to the HMM for the target in question. A popular method used for such a refinement and that utilized here is the Baum–Welch algorithm [22], [23], [43]. While the initial estimates of $\boldsymbol{A}$, $\boldsymbol{B}$, and π are based largely on geometry and *a priori* physical insight, Baum–Welch is a general HMM algorithm removed from the underlying physics and, therefore, it should account for any incorrect assumptions used in our initial probabilities (Baum–Welch only requires initial *estimates* [22], [23], [43] for $\boldsymbol{A}$, $\boldsymbol{B}$, and π, which are readily available from geometry and the underlying physics). Several authors [22], [23], [43], [44] discuss the Baum–Welch

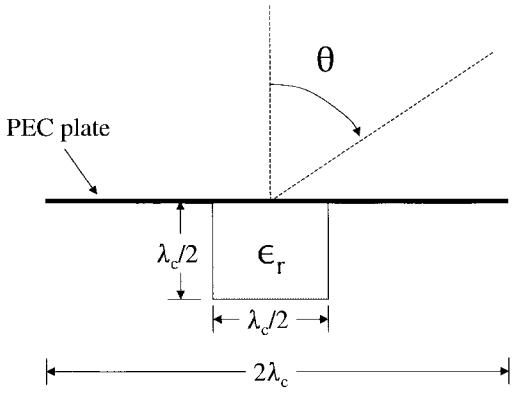

Fig. 3. Two-dimensional canonical target used for the example results. The perfect electric conductor (PEC) is infinitesimally thin and the distance λ_c represents the center wavelength of the incident pulse (Fig. 4). Dielectric constants of $\varepsilon_r = 4$–6 are considered.

algorithm in detail as well as other related algorithms for refining $\boldsymbol{A}$, $\boldsymbol{B}$ and π.

IV. Example Results

The HMM codebook is composed of the wavefront and resonance features characteristic of the targets of interest. If the features representative of the different targets are sufficiently distinct, then those features alone, extracted via wave-based matched pursuits, can be used to effect discrimination. This is implicitly the strategy pursued in resonance-based discrimination, for example, in which the resonant frequencies of the different targets are alone used for discrimination [1]–[4]. However, it is well known that the excitation strength of a given target resonance depends strongly on the target-sensor orientation (hidden in general from the processor) and, therefore, resonances alone are an incomplete tool for discrimination. Similar issues apply with regard to wavefront-based discrimination [6]–[10]. Therefore, the most challenging and realistic scenarios are ones for which the target is characterized by both wavefront and resonance effects with the relative importance of each dependent on the target-sensor orientation. Moreover, the discrimination is further complicated when the particular resonant and wavefront features characteristic of the targets in question are highly correlated. We therefore present examples for the 2-D target in Fig. 3. Ultrawideband backscattered waveforms were computed as a function of target-sensor orientation, assuming TM-polarized plane-wave excitation, with the incident pulse in Fig. 4. The scattered fields were computed via the finite-difference time-domain (FDTD) algorithm [45], [46], considering a Huygen surface for the incident fields [45], [46] a near-to-far-zone transformation [45], [46] and a perfectly matched layer (PML) absorbing boundary [46].

Considering the target in Fig. 3, we note that diffractive scattering from the plate edges will contribute at all incidence angles (the fields are observed in backscatter). Moreover, for angles $90° < \theta < 270°$, resonant scattering from the dielectric slab is expected to be important. To provide a relatively challenging test to the HMM discriminator, we consider three targets of the form in Fig. 3, with each distinguished only by differences in ϵ_r. Here we consider targets with $\epsilon_r = 4$, 5, and 6. We deem this a relatively challenging discrimination problem; matters simplify considerably if the target geometries and electrical parameters are more dramatically different. However, we do not consider this case. When the targets are significantly different, one may no longer require a multiaspect (HMM) processing paradigm since a single scattered waveform (at nearly any orientation) will provide sufficient discrimination. It is felt that this limiting case is rarely found in practice.

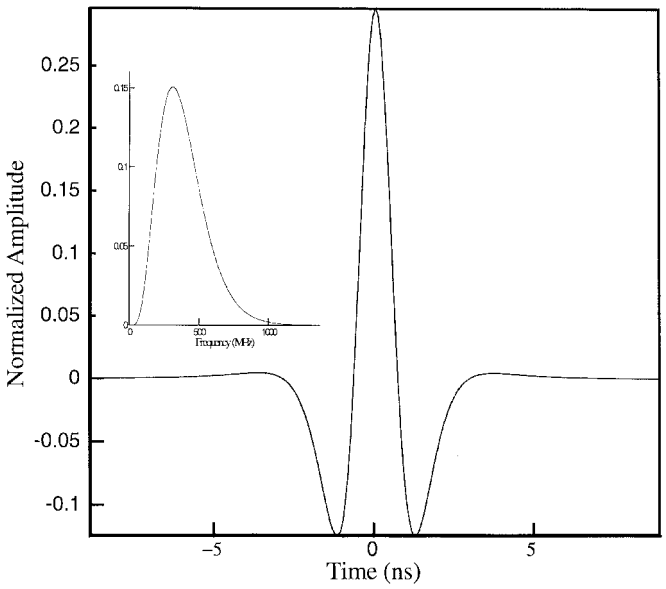

Fig. 4. Incident pulse utilized in the scattering computations (spectrum inset). The frequency spectrum (and associated pulse resolution) are as used in the FDTD [44], [45] computations.

A. Noise-Free Data

As indicated in Fig. 2, the HMM is characterized by multiple states, each of which is representative of an angular (θ) sector over which the scattering phenomenology changes slowly. In general, the underlying physics changes quickly from state to state, while within a given state, the physics is slowly varying. For the target in Fig. 3, with $\epsilon_r = 4$, we found five states (angular sectors) were required to represent the variation in the scattering physics, while when $\epsilon_r = 5$ and $\epsilon_r = 6$, four states were sufficient. As an example of the scattered waveforms and their state-dependent variability, in Fig. 5, we plot an example backscattered waveform from each of the four states characteristic of the $\epsilon_r = 5$ target. For this target, the four states are characterized by $0° \leq \theta \leq 67°$, $67.5° \leq \theta \leq 101°$, $101.5° \leq \theta \leq 150°$, and $150.5° \leq \theta \leq 180°$. From Fig. 5 we note that the different states are characterized by an interesting range of scattering physics, with wavefront scattering playing a principal role for $\theta = 20°$ and $\theta = 65°$ (Fig. 5), and resonances playing an increasing important role for $\theta = 90°$, $\theta = 145°$, and $\theta = 180°$. Similar scattered waveforms exist for the targets with $\epsilon_r = 4$ and $\epsilon_r = 6$. The target with $\epsilon_r = 4$ is characterized by the states $0° < \theta < 72°$, $72.5° < \theta < 100°$, $100.5° < \theta < 136°$, $136.5° < \theta < 153°$, and $153.5° < \theta < 180°$, while the target with $\epsilon_r = 6$ is characterized by the states $0° < \theta < 67°$, $67.5° < \theta < 101°$,

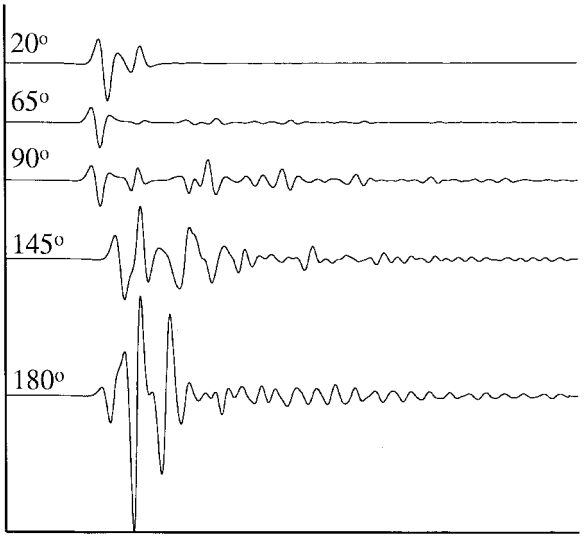

Fig. 5. Example of scattered waveforms from each of the four states characteristic of the target in Fig. 3 ($\epsilon_r = 5$) for the incident pulse in Fig. 4.

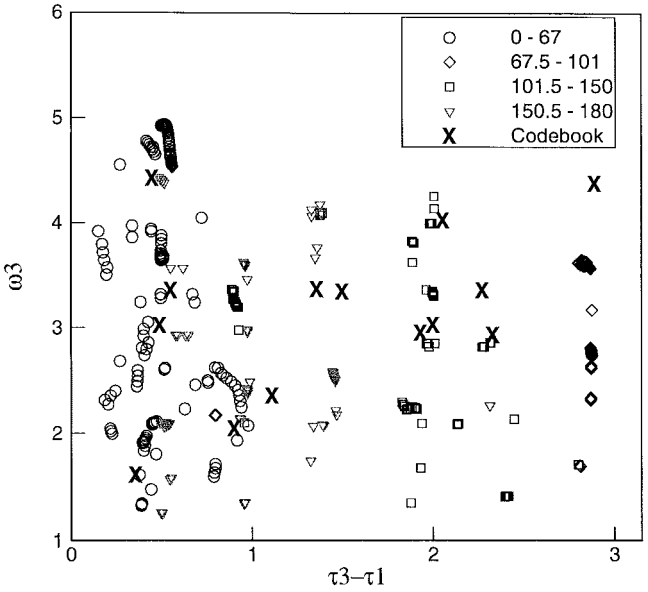

Fig. 6. Matched-pursuits extracted parameters for the target in Fig. 3 ($\epsilon_r = 5$), excited by the incident pulse in Fig. 4. The parameters are projected onto the plane (ω_3, $t_3 - t_1$), with codebook elements depicted by the symbols "X."

$101.5° < \theta < 136°$, and $136.5° < \theta < 180°$. The scattering data was sampled at half-degree angular increments.

Considering Fig. 5, we reiterate that the waveforms scattered at $\theta = 20°$ and $\theta = 60°$ are characterized almost exclusively by edge diffraction with the effects due to the dielectric slab all but nonexistent. Similar effects were witnessed over this angular range for the other two targets. Therefore, if the set of multiaspect backscattered waveforms used to identify the target fall entirely within this range of angles, it will be impossible to distinguish one target from another. This is what we have termed an "ambiguity region," an angular region over which the scattered waveforms from the targets are essentially identical (in principal, there are *some* differences due to diffraction from the dielectric slabs, but these effects are too small to afford reliable discrimination). We will revisit this issue when considering algorithm performance.

As discussed above, the vectors $\boldsymbol{u} = \{\omega_1, \sigma_1, t_2 - t_1, \omega_2, \sigma_2, \cdots, t_K - t_1, \omega_K, \sigma_K\}$ are extracted via wave-based matched pursuits, for each scattered waveform available from a given target. For the examples considered here, we used $K = 3$ matched-pursuits iterations. As an example of the distribution of features characteristic of the target with $\epsilon_r = 5$, in Fig. 6 we depict the extracted vectors $\boldsymbol{u}$ projected onto the $(\omega_3, t_3 - t_1)$ plane of the $3K - 1$ dimensional phase space. In Fig. 6, different symbols are used to denote each of the four states characteristic of this target and the generally clear state partitioning is evident. Also shown in Fig. 6 are the codebook vectors determined via the K-means algorithm [39], projected as well onto the $(\omega_3, t_3 - t_1)$ plane. Note that the codebook vectors generally do a good job of representing the distribution of vectors $\boldsymbol{u}$ in the $(\omega_3, t_3 - t_1)$ plane. However, there are regions in this plane where clusters of vectors $\boldsymbol{u}$ are without an apparent proximate codebook element. This is because the K-means algorithm [39] used to populate the codebook is based on a distance metric in the $3K - 1$ dimensional phase space, where in Fig. 6 we only show projections onto the 2-D $(\omega_3, t_3 - t_1)$ plane.

From Fig. 6 it is seen that at least in the $(\omega_3, t_3 - t_1)$ space, the scattering physics is clearly partitioned into angular sectors (states) over which the relevant physics is relatively slowly varying. This phenomenon naturally suggests the angular sectors used to define the states. We have found this phenomenon—by which the angular-dependent physics naturally defines the states—for all targets considered. However, one could envision a target for which this may not be the case or for which the state partitioning may be less obvious. In this connection, we note that the Baum–Welch [22], [23], [43] scheme refines the initial estimates for the HMM state positions, such that the probability $p(\boldsymbol{O}|\boldsymbol{M})$ in (9) is maximized when the data sequence $\boldsymbol{O}$ corresponds to model $\boldsymbol{M}$. Therefore, the Baum–Welch algorithm refines the initial state partitions as well as the associated probabilities $\boldsymbol{A}$, $\boldsymbol{B}$ and π (see Appendix), such that $p(\boldsymbol{O}|\boldsymbol{M})$ is maximized for the target and model of interest. When the state partitioning is less than obvious, as often the case in speech processing [22], [23], [43], the Baum–Welch algorithm will play an important role. It is worth noting, however, for the targets we have examined thus far, the initial estimates for $\boldsymbol{A}$, $\boldsymbol{B}$ and π (and, implicitly, the state partitions) only changed slightly after refining via the Baum–Welch algorithm.

In Fig. 7, we demonstrate the codebook elements selected as a function of scattered waveform considered (during the training phase, discussed further below). Results are demonstrated for the target with $\epsilon_r = 5$. From this figure, the state definitions are clearly evident (angular sectors over which the physics is slowly varying). Moreover, the anticipated significant interstate variation is pronounced, this playing a critical role in multi-aspect target identification (and in allowing the clear identification of states).

In Fig. 8 we plot the performance of the algorithm as the $-\log[p(\boldsymbol{O}|\boldsymbol{M})]$, such that smaller numbers imply higher probabilities. Recall that the vector $\boldsymbol{O}$ represents the sequence of codebook elements representative of the multi-aspect scattering data sampled. For a given scattered waveform (associated

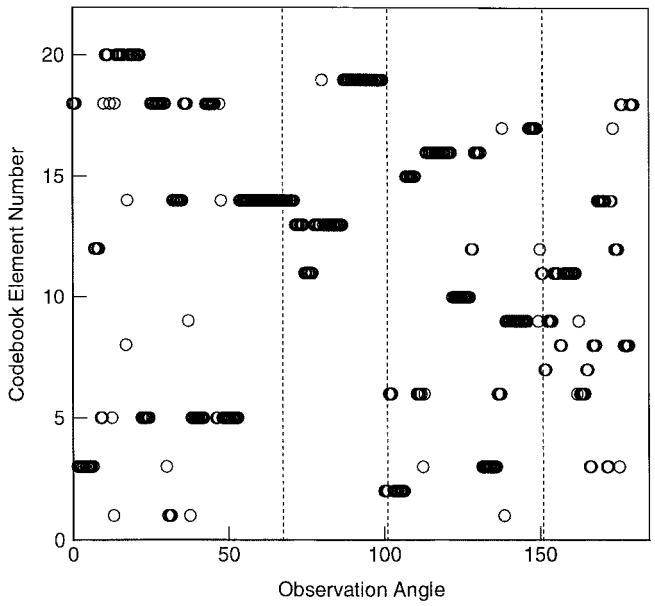

Fig. 7. Codebook elements selected for the target in Fig. 3 ($\epsilon_r = 5$) excited by the pulse in Fig. 4. The codebook elements selected, as a function of angle, tend to naturally suggest a state decomposition (angular sectors over which the underlying physics is relatively slowly varying). The four states used for this target are identified.

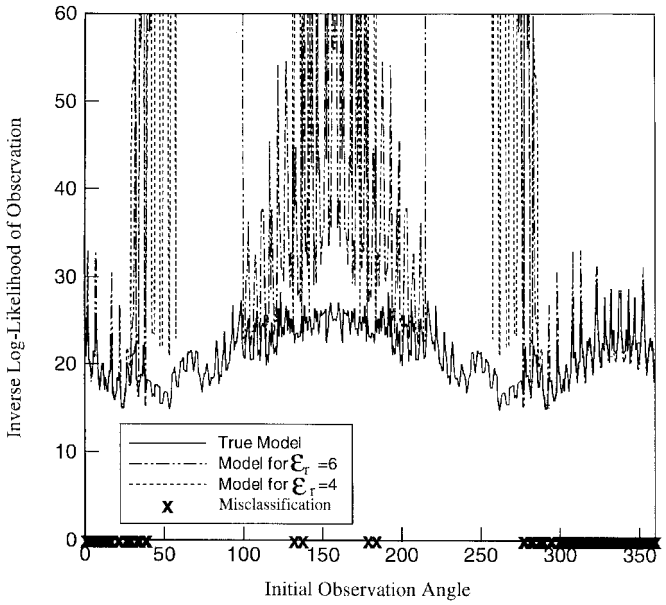

Fig. 8. Algorithm target-discrimination performance with noise-free data coming from the target in Fig. 3, with $\epsilon_r = 5$. Proper classification occurs when the probability of the data being associated with the HMM for $\epsilon_r = 5$ is larger than that for the HMM's for $\epsilon_r = 4$ and 6. Ten scattered waveforms are sampled as a function of angle, using 5° sampling (the FDTD results were computed with 0.5° sampling in angle). Results are plotted in terms of $-\log[p(\boldsymbol{O}|\boldsymbol{M})]$, where $\boldsymbol{M}$ corresponds to each of the three HMM's, with the associated probabilities plotted as a function of the starting angle for each of the sequences of ten waveforms. The HMM's were trained using starting angles with $(n-1)3/2$ degree sampling, with n taking integer values from 1 to 240. Testing was performed using the other 480 starting angles. The "X" symbols identify starting angles for which the associated sequence of scattered waveforms yielded a misclassification.

with one element in $\boldsymbol{O}$), the codebook is determined by first performing wave-based matched pursuits followed by vector quantization [38]–[40]. The vector $\boldsymbol{O}$ therefore represents the results of such for all scattered waveforms in a given sequence (representing a span of target-sensor orientations, where here we consider $M = 10$ scattered waveforms, with 5° angular sampling). We plot $-\log[p(\boldsymbol{O}|\boldsymbol{M}_i)]$ for the three targets discussed above (for three HMM models M_i), where the data actually correspond to that with $\epsilon_r = 5$.

Concerning the results in Fig. 8, the codebook and probabilities $\boldsymbol{A}$, $\boldsymbol{B}$, and π were defined (trained) as follows. We considered a sequence of ten scattered waveforms ($M = 10$), as described above, with the first waveform in each sequence at angle $3(n-1)/2$, for all integers n between 1 and 240 (720 scattered waveforms were available from the FDTD, with a 0.5° sampling interval). The algorithm was tested (after training) using sequences of scattered waveforms (10 waveforms, 5° sampling) with all other starter angles (480 sets). In this manner, all 720 scattered waveforms were examined when deriving the codebook and estimating $\boldsymbol{A}$, $\boldsymbol{B}$, and π, but the sequences used for testing were different than those used for training. Finally, note that although the target is symmetrtic about $\theta = 0°$ and $\theta = 180°$, a sequence with starting angle at $\theta = 90°$ (for example) is not the same as one for starting angle $\theta = 270°$ (the direction of the state transitions are reversed).

From Fig. 8 we see that for most initial angles (abscissa), $p(\boldsymbol{O}|\boldsymbol{M}_k) > p(\boldsymbol{O}|\boldsymbol{M}_i)$ for $i \neq k$, where $\boldsymbol{M}_k$ is the HMM for the data under test (corresponding to the target with $\epsilon_r = 5$). However, there are several initial angles for which this is not the case (marked in Fig. 8 with an "X"). These identification failures occur when all of the ten scattered waveforms used to generate $\boldsymbol{O}$ reside in the aforementioned "ambiguity region." For these sequences of measured waveforms, the underlying physics is virtually independent of the dielectric slab (the incident fields being largely shielded from the slab by the perfectly conducting plate). In fact, for starting angles in this ambiguity region any correct identification is largely serendipity and can be ignored as meaningless. From Fig. 8, we define the ambiguity region as (initial angles) lying between 0, 40, 280, and 360°. For the $M = 10$ waveforms considered, at a 5° sampling (45° angular swath), this ambiguity region implies that backscattered waveforms in the region 275–360 and 0–85° are very weakly influenced by the presence of the dielectric slab and, therefore, it is virtually impossible to discriminate between the targets based solely on backscattered waveforms in this region. If at least some of the ten waveforms reside outside of this region (starting angle outside the ambiguity region), discrimination is possible.

An additional interesting phenomenon is evident from consideration of Fig. 8. In particular, note that the greatest discrimination performance [differences in $p(\boldsymbol{O}|\boldsymbol{M}_i)$] occurs for starting angles in the vicinity of $\theta = 90°$ and $\theta = 270°$. This is explained as follows. For TM-polarized excitation at these angles, there is no diffraction from the perfectly conducting plate alone in the absence of the dielectric slab. Therefore, at and around these incidence angles and for the TM excitation considered, scattering due to the conducting plate is expected to be reduced (it is not eliminated entirely, for the fields scattered from the slab must interact with the plate). Hence, at and around these angles the scattered fields are dominated by that portion of the *general* target in Fig. 3 (the slab)

TABLE I
PROBABILITY OF MISCLASSIFICATION FOR EACH OF THE THREE TARGETS (THE TARGET IN FIG. 3, WITH $\epsilon_r = 4$–6). NOISE-FREE RESULTS ARE SHOWN, FOR SEQUENCE LENGTHS OF $M = 10$, 5 AND 2 SCATTERED WAVEFORMS (5° ANGULAR SAMPLING). THE TRAINING AND TESTING WERE PERFORMED AS DISCUSSED IN THE CAPTION TO FIG. 8 AND RESULTS ARE PRESENTED FOR CASES IN WHICH AT LEAST ONE SCATTERED WAVEFORM IN THE SEQUENCE IS OUTSIDE THE "AMBIGUITY REGION" (THE ANGULAR REGION IN WHICH THE SCATTERED WAVEFORMS FROM ALL THREE TARGETS ARE VIRTUALLY INDISTINGUISHABLE). THE MISCLASSIFICATION PROBABILITY IS THE PROBABILITY THAT DATA FROM A GIVEN TARGET IS ASSOCIATED WITH A HMM CHARACTERISTIC OF A DIFFERENT TARGET. THE RESULTS HERE ARE AVERAGED ACROSS ALL THREE TARGETS CONSIDERED

	Sequence Length = 10	Sequence Length = 5	Sequence Length = 2
$\varepsilon_r = 4$	3.8	5.7	8.2
$\varepsilon_r = 5$	1.3	14.3	35.8
$\varepsilon_r = 6$	0.65	7.1	23.5

that distinguishes the *particular* three targets considered. It is in this region that an algorithm should provide optimal discrimination. In practice, however, one cannot count on exploiting such a propitious target-sensor orientation since such is generally hidden from the processor.

In Table I, we give the probability of misclassification for each of the three targets. Results are shown for testing as discussed, using sequence lengths of $M = 10$, 5, and 2 scattered waveforms (in each case there is 5° angular sampling between waveforms). For the reasons discussed, algorithm performance is only scored for initial angles outside the ambiguity region where such is meaningful. Despite the fact that testing and training were performed on different sequences, we see from Table I that classification performance is quite good for large data sequences ($M = 10$ observation-dependent scattered waveforms). As expected, as the number of scattered waveforms is reduced ($M = 5$ and $M = 2$), classification performance deteriorates.

C. Noisy Data

In the final set of examples, we consider the same scattering data addressed above with additive white Gaussian noise. Overall performance is dependent on the ability of the wave-based matched-pursuits algorithm to accurately extract features (wavefronts and resonances) from noisy data. This issue has been addressed in a previous paper [37] and is summarized briefly here.

For a scattered waveform $\boldsymbol{f}$ with additive white Gaussian noise $\boldsymbol{w}$, we process the signal $\boldsymbol{s} = \boldsymbol{f} + \boldsymbol{w}$. For a matched-pursuits dictionary composed of elements $\boldsymbol{e}_n \equiv \boldsymbol{e}(\gamma_n)$, we compute inner products $\langle \boldsymbol{s}|\boldsymbol{e}_n\rangle$ with each element in the dictionary and select the largest inner product. As discussed in Section II, the process is subsequently and iteratively repeated on the remainder. The inner products satisfy $\langle \boldsymbol{s}|\boldsymbol{e}_n\rangle = \langle \boldsymbol{f}|\boldsymbol{e}_n\rangle + \langle \boldsymbol{w}|\boldsymbol{e}_n\rangle$. The $\langle \boldsymbol{w}|\boldsymbol{e}_n\rangle$ are zero-mean Gaussian random variables with variance σ^2, where σ^2 is the variance of the noise $\boldsymbol{w}$. If the variance σ^2 is large relative to $|\langle \boldsymbol{f}|\boldsymbol{e}_n\rangle|^2$, for all $\boldsymbol{e}_n$ in the dictionary, then the algorithm will have difficulty extracting the underlying signal from the additive noise. Therefore, in the context of matched pursuits, the figure of merit for noisy data is what we have termed the signal-component signal-to-noise ratio [37] (SC-SNR) defined as $|\langle \boldsymbol{f}|\boldsymbol{e}_n\rangle|^2/\sigma^2$. Therefore, the SNR is dependent on the target feature (signal component) in question defined as $|\langle \boldsymbol{f}|\boldsymbol{e}_n\rangle|^2/\sigma^2$, where $\boldsymbol{e}_n$ represents the dictionary element (feature) extracted via matched pursuits in the *absence* of additive noise. The SC-SNR must be reasonably large (on the order of 5 dB or greater [37]) for at least some dictionary elements, for matched pursuits to work properly. For the noisy examples considered here, we consider an SC-SNR of greater than or equal to 10 dB (i.e., $|\langle \boldsymbol{f}|\boldsymbol{e}_n\rangle|^2/\sigma^2 \geq 10$ for all $\boldsymbol{e}_n$ selected for representation of $\boldsymbol{f}$, after K matched-pursuits iterations, in the *absence* of noise). Hence, many of the signal components $\boldsymbol{e}_n$ have an associated SC-SNR well in excess of 10 dB. In Fig. 9, are plotted the same scattered waveforms shown in Fig. 5, with example realizations of additive noise at the noise variance considered. As expected, the SNR (and SC-SNR) depends strongly on the target-sensor orientation.

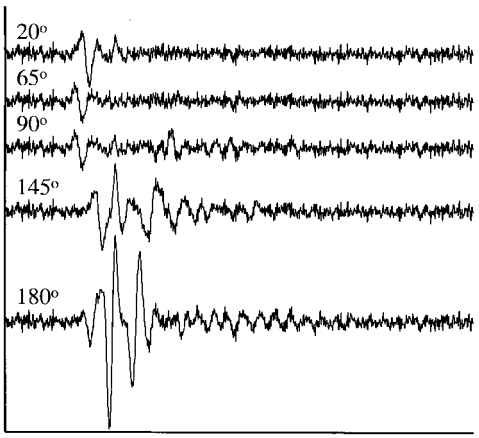

Fig. 9. The same state-dependent scattered waveforms as plotted in Fig. 5, with a minimum of 10-dB SC-SNR additive white Gaussian noise.

For noisy data $\boldsymbol{s} = \boldsymbol{f} + \boldsymbol{w}$, we train the HMM algorithm by considering consecutive sets of M scattered waveforms at a prescribed angular sampling rate with the initial angle of observation varied. For each of the 720 scattered waveforms $\boldsymbol{f}$ available for each target (0.5° angular sampling), we generate an associated noise waveform $\boldsymbol{w}$ with each $\boldsymbol{w}$ different but described by the same statistical distribution. This process is done eight times (5760 realizations of $\boldsymbol{w}$), and the HMM probabilities $\boldsymbol{A}$, $\boldsymbol{B}$, and π are trained (and the code books generated) using all 5760 initial angles. The algorithm is tested by considering all possible initial observation angles (720), with four (different) realizations of the noise $\boldsymbol{w}$ at each angle (a total of 2880 testing sequences, each of length M). Therefore, the data $\boldsymbol{s}$ used for HMM training is different than that used for testing, although the underlying signal $\boldsymbol{f}$ and the noise statistics are the same.

The probability of misclassification for the noisy data (minimum SC-SNR of 10 dB) is presented in Table II in the same form as considered in Table I. Comparing Tables I and II, we see that the presence of noise at the noise levels

TABLE II
AS IN TABLE I, WITH AT LEAST 10-dB SC-SNR ADDITIVE WHITE GAUSSIAN NOISE (SEE FIG. 9). THE TESTING AND TRAINING WERE PERFORMED WITH DIFFERENT ADDITIVE-NOISE REALIZATIONS (EACH REPRESENTATIVE OF THE SAME NOISE STATISTICS)

	Sequence Length = 10	Sequence Length = 5	Sequence Length = 2
$\epsilon_r = 4$	1.9	3.5	10.3
$\epsilon_r = 5$	6.5	9.2	24.7
$\epsilon_r = 6$	4.0	7.0	25.2

TABLE III
COMPARISON OF HMM CLASSIFICATION PERFORMANCE FOR NOISY DATA ($M = 10$ SCATTERED WAVEFORMS, 5° SAMPLING) USING THE FULL MATCHED-PURSUITS DICTIONARY [SEE (4) AND (5)] AND USING A CONSTRAINED MATCHED-PURSUITS DICTIONARY "LEARNED" BY INITIALLY APPLYING THE MATCHED-PURSUITS ALGORITHM TO NOISE-FREE DATA

	Unconstrained MP dictionary	Constrained MP dictionary
$\epsilon_r = 4$	1.9	2.7
$\epsilon_r = 5$	6.5	9.0
$\epsilon_r = 6$	4.0	4.7

considered does not cause a dramatic deterioration in algorithm performance (for data length $M = 10$). In fact, for the $M = 10$ case, the results are actually better *with* noise. This is simply because, as mentioned previously, more extensive training can be implemented for noisy data than for the finite set of noise-free data (also, for the noise-free case, we tested and trained on different scattered waveform sequences). As the noise variance increases, a more pronounced performance deterioration is anticipated. It is interesting to note that in both Tables I and II, the target with $\epsilon_r = 5$ is generally characterized by the highest level of misclassification. This is to be expected, for it has two neighboring targets with very similar electrical parameters ($\epsilon_r = 4$ and $\epsilon_r = 6$) to which it can be misclassified, where the targets with $\epsilon_r = 4$ and $\epsilon_r = 6$ only have one such target with proximate electrical properties.

The final issue we address concerns the matched-pursuits dictionary D, defined in (4) and (5). If one has access to the *noise-free* scattered waveforms $\boldsymbol{f}$ characteristic of a given target, one can apply matched pursuits to $\boldsymbol{f}$ and determine the set of vectors D' ($D' \subset D$) that are representative of the data (it is the vectors in D' that we used to define the aforementioned SC-SNR). One could envision access to noise-free model or measured data that can be used via matched pursuits to learn D' and then the reduced dictionary D' can be applied to the noisy data (with known or estimated statistics). This strategy has several salutary features. First, the reduced dictionary D' is generally much smaller than the original dictionary D. Therefore, use of the smaller dictionary D' with the HMM results in a significant acceleration in algorithm speed. Moreover, the matched-pursuits dictionary D' is, through training on noise-free data, well matched to the underlying signal $\boldsymbol{f}$ and, therefore, is more robust for processing noisy data $\boldsymbol{s} = \boldsymbol{f} + \boldsymbol{w}$ than the original dictionary D. For the results presented in Table II we have utilized the reduced dictionary D' rather than the original dictionary D described in (4) and (5). For the data considered here, D' has 85 elements while the original dictionary has 996, yielding significant algorithm acceleration. Moreover, as demonstrated in Table III, the reduced dictionary D' manifests HMM performance (for the noisy data) that is significantly better than that when the full (original) dictionary D is applied. This is expected, for dictionary elements in D that are matched to the noise but not to $\boldsymbol{f}$ are not found in the reduced dictionary D'.

V. CONCLUSIONS

In this paper, we have considered the use of scattered electromagnetic fields for the identification of a concealed or hidden target. Previous solutions to this problem have been pursued in terms of wavefront [1]–[4] and resonance-based [5]–[10] processing. While each approach has met with some success, it is well known that the fields scattered from a general target must be described simultaneously in terms of wavefronts and resonances [18], with the relative importance of each dictated by the details of the underlying wave physics. Moreover, motivated in large part by observed mammalian target-identification procedures [30]–[32], we have sought the development of an algorithm that employs a multi-aspect paradigm, wherein the scattered fields from multiple target-sensor orientations are processed simultaneously (i.e., fused) to effect target discrimination. In addition to being representative of target discrimination in nature, this approach mitigates the difficulties of a single-aspect scheme that has severe limitations for targets that have a complicated aspect-dependent signature. Finally, the multi-aspect paradigm is consistent with data acquisition procedures used in SAR [33], ISAR [34], and inverse scattering [35].

As detailed in the text, each of the multi-aspect time-domain waveforms is parsed in terms of wavefronts and resonances via the wave-based matched-pursuits algorithm. The continuous parameters representative of each such parametric decomposition are then mapped into one element in a finite codebook of such parameters through VQ. Thus, after matched-pursuits parametric data parsing and VQ, the sequence of multi-aspect scattered waveforms are represented in terms of an associated sequence of codebook elements. A hidden Markov model (HMM) is defined for each target of interest and that HMM for which the sequence of codebook element gives the highest probability of occurrence is deemed the HMM representative of the target under interrogation (thus identifying the target).

The probability of observing a given codebook element for a particular target is dependent on the target-sensor orientation since such dictates the associated scattering physics. Thus, "states" are defined, representative of particular target-sensor orientations over which the underlying physics (and, hence, the probability of observing a given codebook element) is relatively slowly varying. The multi-aspect scattered fields are

modeled as a Markovian process of state transitions; a *hidden* Markov process because the underlying states are concealed from the processor with the absolute target-sensor orientation unknown.

The general paradigm has been illustrated here using computed scattering data from three very similar targets. Analogous results have been presented elsewhere for measured acoustic scattering data from submerged elastic targets [46]. However, several issues warrant further consideration and development. In particular, we first note that we have assumed that the state-transition probabilities quantified by the matrix $\boldsymbol{A}$ are time-independent. In reality, however, this is not the case. Previous history plays an important role in the state-transition probabilities. For example, assume state $\boldsymbol{S}_i$ has an angular extent of 8° and 5° angular sampling is used. If the sensor-target orientation is in state $\boldsymbol{S}_i$ on two consecutive observations, the probability of transitioning out of this state is 100%. This is different from the transition probability if one is only in state $\boldsymbol{S}_i$ for one observation. Similar issues have been addressed in speech processing [26] and will be considered here as well in the context of target identification.

Another issue involves the form of the HMM applied here in which a *discrete* and finite codebook has been utilized (leading to the matrix $\boldsymbol{B}$, representing the probabilities of observing in a given state each of the finite set of codebook elements). Alternatively, one could employ a *continuous* HMM, in which probabilities are attached to observing the continuous matched-pursuits parameters, without VQ. Continuous HMM's have received considerable attention in speech processing [22], [23], [40] and warrant attention in the context of target identification.

Finally, here we have applied matched pursuits and the associated HMM directly in the time-domain data domain. In the context of SAR or ISAR, one may rather employ this technique in the 2-D image domain. This would imply generating multiple 2-D images, utilizing subsections (subapertures) of the full synthetic-aperture data set from which the target and environment will be viewed from multiple orientations. In this scenario, 2-D physics-based matched-pursuits dictionary elements are required. However, the basic HMM construct remains unchanged. The application of this algorithm to SAR and ISAR data constitutes the principal direction of our current research.

APPENDIX
INITIAL ESTIMATION OF $\boldsymbol{A}$, $\boldsymbol{B}$, AND π

Assume that a given target can be represented by M_s contiguous states, with (in two dimensions) consecutive angular support of $\theta_1, \theta_2, \cdots, \theta_{M_s}$, denoted by states $\boldsymbol{s} = \{s_1, s_2, \cdots, s_{M_s}\}$, respectively. Further, let $q_m \in \boldsymbol{s}$ represent the hidden state sampled by the mth observed scattered waveform. If the target orientation is assumed uniformly distributed, the initial-state probabilities are defined as

$$\pi_k \equiv P(q_1 = s_k) = \frac{\theta_k}{\sum_{k=1}^{M_s} \theta_k}. \tag{A.1}$$

Moreover, if we assume that the sensor moves in one direction relative to the putative target center (the target has been detected, and is now being identified) with angular sampling $\Delta\theta$, with $\Delta\theta < \theta_k \,\forall\, \theta_k$, then the probability of transitioning from state i to state k, represented by $A_{ik} \equiv P(q_{m+1} = s_k | q_m = s_i)$ is given by

$$\begin{aligned} A_{ik} &= \frac{\theta_i - \Delta\theta}{\theta_i}, && \text{if } i = k \\ A_{ik} &= \frac{\Delta\theta}{2\theta_i}, && \text{if } |i-k| = 1 \\ A_{ik} &= 0, && \text{if } |i-k| > 1. \end{aligned} \tag{A.2}$$

Like (A.1), the expressions in (B.1) are derivable directly from geometrical considerations. Considering A_{ii}, for example, assume that scattered waveform m is uniformly likely to be located at any angle in state i. There are a range of angles θ_i–$\Delta\theta$ for which a change in the target-sensor orientation of $\Delta\theta$ will yield a target-sensor orientation that still resides with state i. We therefore have $A_{ii} = (\theta_i – \Delta\theta)/\theta_i$. The other terms in (A.2) are derived similarly.

The matrix $\boldsymbol{B}$ is computed by considering all the training data available for state k of a given target. The probability that codebook element i is selected for state k is given by

$$B_{ik} = \frac{n_{ik}}{n_k} \tag{A.3}$$

where n_k is the total number of training waveforms for state k, and n_{ik} represents the number of times codebook element i was selected for such.

ACKNOWLEDGMENT

The authors would like to thank their colleague T. Dogaru who provided the FDTD computed scattered fields.

REFERENCES

[1] C. E. Baum, "The singularity expansion method," in *Transient Electromagnetic Fields*, L. B. Felsen, Ed. New York: Springer-Verlag, 1976.
[2] E. Heyman and L. B. Felsen, "A wavefront interpretation of the singularity expansion method," *IEEE Trans. Antennas Propagat.*, vol. AP-33, pp. 706–718, July 1985.
[3] K.-M. Chen, D. P. Nyquist, E. J. Rothwell, L. L. Webb, and B. Drachman, "Radar target discrimination by convolution of radar return with extinction-pulses and single-mode extraction signals," *IEEE Trans. Antennas Propagat.*, vol. AP-34, pp. 896–904, July 1986.
[4] A. J. Poggio, M. L. Van Blaricum, E. K. Miller, and R. Mittra, "Evaluation of a processing technique for transient data," *IEEE Trans. Antennas Propagat.*, vol. AP-26, pp. 165–173, Jan. 1978.
[5] J. B. Keller, "Geometrical theory of diffraction," *J. Opt. Soc. Amer.*, vol. 52, pp. 116–130, Feb. 1962.
[6] M. McClure, R. C. Qiu, and L. Carin, "On the super-resolution identification of observables from swept-frequency scattering data," *IEEE Trans. Antennas Propagat.*, vol. 45, pp. 631–641, Apr. 1997.
[7] R. A. Atles, "Sonar for generalized target description and it's similarity to animal echolocation systems," *J. Acoust. Soc. Amer.*, vol. 59, pp. 97–105, Jan. 1976.
[8] M. P. Hurst and R. Mittra, "Scattering center analysis via Prony's method," *IEEE Trans. Antennas Propagat.*, vol. AP-35, pp. 986–988, Aug. 1987.
[9] R. Carrierre and R. L. Moses, "High resolution parametric modeling of canonical radar scatterers with application to target identification," *IEEE Trans. Antennas Propagat.*, vol. 40, pp. 13–18, Jan. 1992.
[10] W. M. Steedly and R. L. Moses, "High resolution exponential modeling of fully polarized radar returns," *IEEE Trans. Aerosp. Electron. Syst.*, vol. 27, pp. 459–469, May 1991.

[11] A. Moghaddar and E. K. Walton, "Time-frequency distribution analysis of scattering from waveguide cavities," *IEEE Trans. Antennas Propagat.*, vol. 41, pp. 677–680, May 1993.
[12] H. Kim and H. Ling, "Wavelet analysis of back-scattering data from an open-ended waveguide cavity," *IEEE Microwave Guided Wave Lett.*, vol. 2, p. 140–142, Apr. 1992.
[13] D. R. Kralj, M. McClure, L. Carin, and L. B. Felsen, "Time domain wave-oriented data processing for scattering by nonuniform truncated gratings," *J. Opt. Soc. Amer.*, vol. 11, pt. A, pp. 2685–2694, Oct. 1994.
[14] G. C. Gaunaurd, H. C. Strifors, A. Abrahamsson, and B. Brusmark, "Scattering of short EM-pulses by simple and complex targets using impulse radar," in *Ultra-Wideband Short-Pulse Electromagnetics*, H. L. Bertoni, L. Carin, and L. B. Felsen, Eds. New York: Plenum, 1993, pp. 437–444.
[15] L. Carin and L. B. Felsen, "Wave-oriented data processing for frequency and time domain scattering by nonuniform truncated array," *IEEE Antennas Propagat. Mag.*, vol. 36, pp. 29–43, June 1994.
[16] H. Kim and H. Ling, "Wavelet analysis of radar echo from finite size targets," *IEEE Trans. Antennas Propagat.*, vol. 41, pp. 200–207, Feb. 1993.
[17] L. Carin, L. B. Felsen, D. R. Kralj, H. S. Oh, W. C. Lee, and S. U. Pillai, "Wave-oriented data processing of dispersive time-domain scattering data," *IEEE Microwave Guided Wave Lett.*, vol. 45, pp. 592–600, Apr. 1997.
[18] M. McClure and L. Carin, "Matched pursuits with a wave-based dictionary," *IEEE Trans. Signal Processing*, vol. 45, pp. 2912–2927, Dec. 1997.
[19] L. C. Trintinalia and H. Ling, "Joint time-frequency ISAR using adaptive processing," *IEEE Trans. Antennas Propagat.*, vol. 45, pp. 221–227, Feb. 1997.
[20] S. G. Mallat and Z. Zhang, "Matched pursuits with time-frequency dictionaries," *IEEE Trans. Signal Processing*, vol. 41, pp. 3397–3415, Dec. 1993.
[21] S. E. Levinson, " Structural methods in automatic speech recognition," *Proc. IEEE*, vol. 73, pp. 1625–1650, Nov. 1985.
[22] L. R. Rabiner and B. H. Juang, "An introduction to hidden Markov models," *IEEE Acoust., Speech, Signal Processing Mag*, vol. 3, pp. 4–16, Jan. 1986.
[23] L. R. Rabiner, "A tutorial on hidden Markov models and selected applications in speech recognition," *Proc. IEEE*, vol. 77, pp. 257–285, Feb. 1989.
[24] J. Picone, "Continuous speech recognition using hidden Markov models," *IEEE Acoust., Speech, Signal Processing Mag.*, vol. 7, pp. 26–41, July 1990.
[25] S. Young, "A review of large-vocabulary continuous speech recognition," *IEEE Signal Processing Mag.*, vol. 13, pp. 45–57, Sept. 1996.
[26] S. E. Levinson, "Continuously variable duration hidden Markov models for automatic speech recognition," *Comput, Speech, Language*, vol. 1, pp. 29–45, Mar. 1986.
[27] C. H. Lee and L. R. Rabiner, "A frame-synchronous network search algorithm for connected word recognition," *IEEE Trans. Acoust., Speech, Signal Processing*, vol. 37, pp. 1649–1658, Nov. 1989.
[28] R. Bakis, "Continuous speech word recognition via centisecond acoustic states," in *Proc. 91st Annu. Meet. Acoustical Soc. Amer.*, Washington, DC, 1976.
[29] B. S. Atal, "Effectiveness of linear prediction characteristics of the speech wave for automatic speaker identification and verification," *J. Acoust. Soc. Amer.*, vol. 55, pp. 1304–1312, 1974.
[30] J. A. Simmons, P. A. Saillant, and S. P. Dear, "Through a bat's ear," *IEEE Spectrum*, vol. 29, pp. 46–48, Mar. 1992.
[31] J. A. Simmons, M. Ferragamo, C. F. Moss, S. B. Stevenson, R. A. Altes, "Discrimination of jittered sonar echoes by the echo-locating bat, Eptesicus fuscus: The shape of target images in echolocation," *J. Comp. Physiol. A*, vol. 267, pp. 589–616, 1990.
[32] J. A. Simmons, "A view of the world through the bat's ear: The formation of acoustic images in echolocation," *Cognition*, vol. 33, pp. 155–199, 1989.
[33] R. O. Harger, *Synthetic Aperture Radar Systems.* New York: Academic, 1970, pp. 104–107.
[34] J. L. Walker, "Range-Doppler imaging of rotating objects," *IEEE Trans. Aerosp. Electron. Syst.*, vol. AES-16, pp. 23–52, Jan. 1980.
[35] W. C. Chew, *Waves and Fields in Inhomogeneous Media* New York: Oxford, 1996, ch. 9.
[36] S. Grossberg, H. Hawkins, and A. Waxman, Eds., *Neural Networks, Special Issue: Neural Network for ATR*, vol. 8, 1995.
[37] M. McClure and L. Carin, "Wave-based matching-pursuits detection of submerged elastic targets," *J. Acoust. Soc. Amer.*, vol. 104, pt. 1, pp. 937–946, Aug. 1998.
[38] J. Makhoul, S. Raucos, and H. Gish, "Vector quantization in speech coding," *Proc. IEEE*, vol. 73, pp. 1551–1558, Nov. 1985.
[39] Y. Linde, A. Buzo, and R. M. Gray, "An algorithm for vector quantizer design," *IEEE Trans. Communicat.*, vol. 28, pp. 84–95, Jan. 1980.
[40] J. Deller, J. Proakis, and J. Hansen, *Discrete-Time Processing of Speech Signals.* Englewood Cliffs, NJ: Prentice-Hall, 1993.
[41] L. L. Scharf, *Statistical Signal Processing, Detection, Estimation, and Time Series Analysis.* New York: Addison-Wesley, 1990.
[42] P. R. Runkle, P. K. Bharadwaj, L. Couchman, and L. Carin, "Hidden Markov models for multiaspect target classification," *IEEE Trans. Signal Processing*, vol. 47, pp. 2035–2040, July 1999.
[43] L. E. Baum, T. Petrie, G. Soules, and N. Weiss, "A maximization technique occurring in the statistical analysis of probabilistic functions of Markov chains," *Ann. Math. Statistics*, vol. 41, pp. 164–171, 1970.
[44] A. Viterbi, "Error bounds for convolutional codes and an asymptotically optimum decoding algorithm," *IEEE Trans. Inform. Theory*, vol. 13, pp. 260–269, Apr. 1967.
[45] Kunz and R. J. Luebbers, *The Finite Difference Time Domain Method for Electromagnetics.* Boca Raton, FL: CRC, 1993.
[46] A. Taflove, *Computational Electrodynamics; The Finite-Difference Time-Domain Method.* Norwood, MA: Artech House, 1995.

Priya K. Bharadwaj received the B.Tech degree from Regional Engineering College, Warangal, India, in 1996, and the M.S. degree from the Department of Electrical and Computer Engineering, Duke University, in 1998. She is currently working toward the Ph.D. degree at Duke University.

Her research interests include statistical signal processing and related applications.

Paul R. Runkle received the B.S. degree in applied mathematics and physics from the University of Wisconsin, Madison, in 1988, and the M.S. degree in electrical engineering from the University of Michigan, Ann Arbor, MI, in 1992. He is currently working toward the Ph.D. degree.

Since 1998, he has been a Research Associate in the Department of Electrical and Computer Engineering, Duke University, Durham, NC. His research interests include statistical signal processing and modeling, multichannel signal processing, image processing, and related applications.

Lawrence Carin (SM'96) was born March 25, 1963, in Washington, DC. He received the B.S., M.S., and Ph.D. degrees in electrical engineering, all from the University of Maryland, College Park, in 1985, 1986, and 1989, respectively.

In 1989, he joined the Electrical Engineering Department, Polytechnic University, Brooklyn, NY, as an Assistant Professor and became an Associate Professor there in 1994. In September 1995, he joined the Electrical Engineering Department at Duke University, where he is an Associate Professor. His current research interests include short-pulse scattering, subsurface sensing, and wave-based signal processing.

Dr. Carin is currently an Associate Editor of the IEEE TRANSACTIONS ON ANTENNAS AND PROPAGATION. He is a member of the Tau Beta Pi and Eta Kappa Nu honor societies.